Rheology of FIG inks
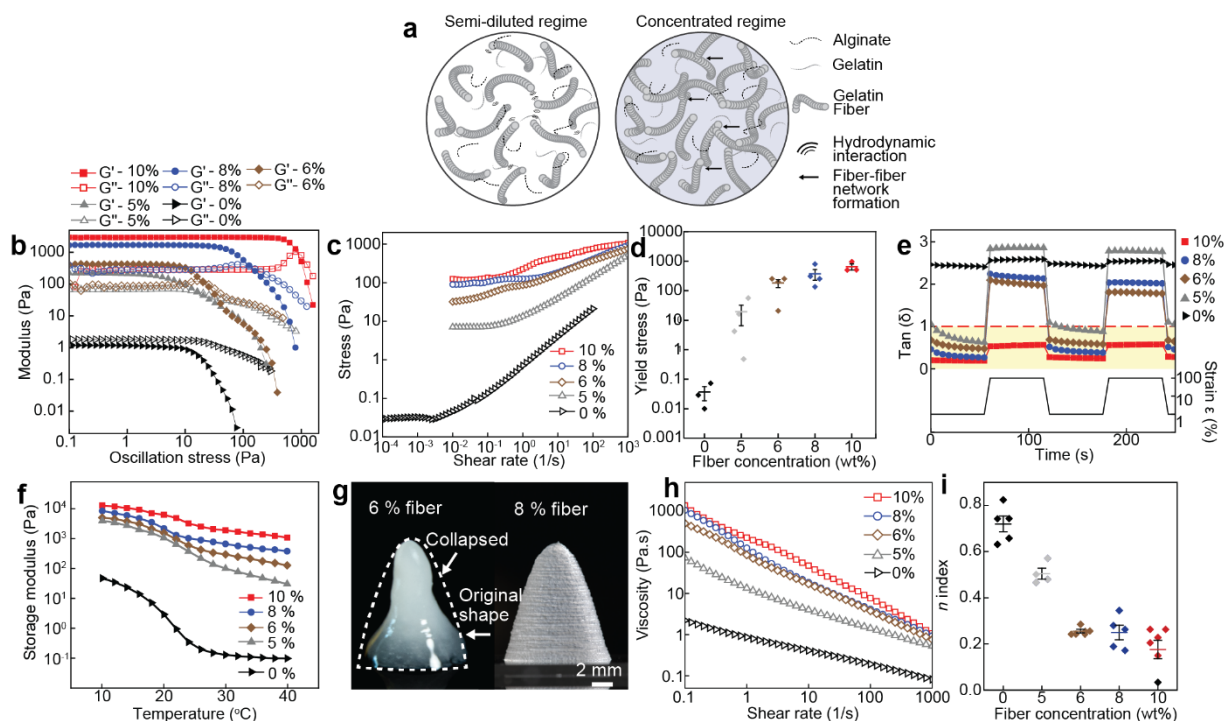
The rheological properties of the FIG ink were highly influenced by fiber packing density in the polymer matrix. To investigate the effective fiber concentrations that enabled the printing of 3D scaffolds with accurate shape retention and preservation of the fiber alignment, we evaluated the rheological properties of FIG inks consisting of a blended gelatin/alginate hydrogel (2.4 wt% gelatin and 2.4 wt% alginate) infused with either 0, 5, 6, 8, or 10 wt% of fibers. At higher fiber concentrations, random movement of high aspect ratio fibers becomes reduced, as fiber-fiber contact interaction is increased[1, 2]. As the fibers are densely packed, the fiber-fiber contact interaction becomes dominant over fiber-fluid interaction (Supplementary Fig. 2a), conferring high viscosity and solid-like behavior of FIG inks[1]. Consequently, the FIG inks with a higher fiber concentration showed elastic properties at rest.

To assess these viscoelastic properties of FIG inks, we measured their dynamic modulus (Elastic storage modulus, G′ and viscous loss modulus, G′′, representing elastic and viscous response, respectively) as a function of oscillation stress (Fig. 1e, and Supplementary Fig. 2b). At 0 wt% fiber, the loss modulus was higher than the storage modulus within the tested range of applied shear stress (0.1 Pa-1000 Pa), indicative of a liquid-like behavior (Supplementary Fig. 2b) as a result of low yield stress (Supplementary Fig. 2d). In contrast, FIG inks show higher storage modulus than loss modulus, indicating solid-like behavior at rest (Supplementary Fig. 2b). During printing, the FIG inks flow as the they experience shear stress above the yield stress corresponding to the crossover point of G' and G" (Supplementary Fig. 2b). While the FIG inks flow, fibers were aligned by shear stress at the nozzle[1], resulting in a decrease in viscosity (i.e. shear thinning behavior) (Supplementary Fig. 2h). To quantitatively assess shear-thinning behavior, we used the power-law model, which is defined as $\eta(\dot{\gamma}) = K\dot{\gamma}^{n-1}$, where η is viscosity, K is consistency index

(defined as the viscosity at the shear rate of 1 s^{-1}), $\dot{\gamma}$ is the shear rate, and n is the shear-thinning index. When n is lower than 1, inks show shear-thinning behavior, and the ink with lower n has stronger shear-thinning behavior. The n indexes were derived from the viscosity-shear rate graph using the power-law equation (Supplementary Fig. 2h). The higher fiber concentration of the FIG inks showed a stronger shear thinning behavior (Supplementary Fig. 2h-i). After FIGs inks were extruded out, they restored solid-like behavior quickly as demonstrated by the rapid response of crossover between storage and loss modulus under alternating small (1 %) or large (100 %) magnitudes of oscillation strains applied to the inks (Supplementary Fig. 2e). Quick and reversible gelation that occurs for the start/stop events of printing, allows for the preservation of shear-induced fiber alignment.
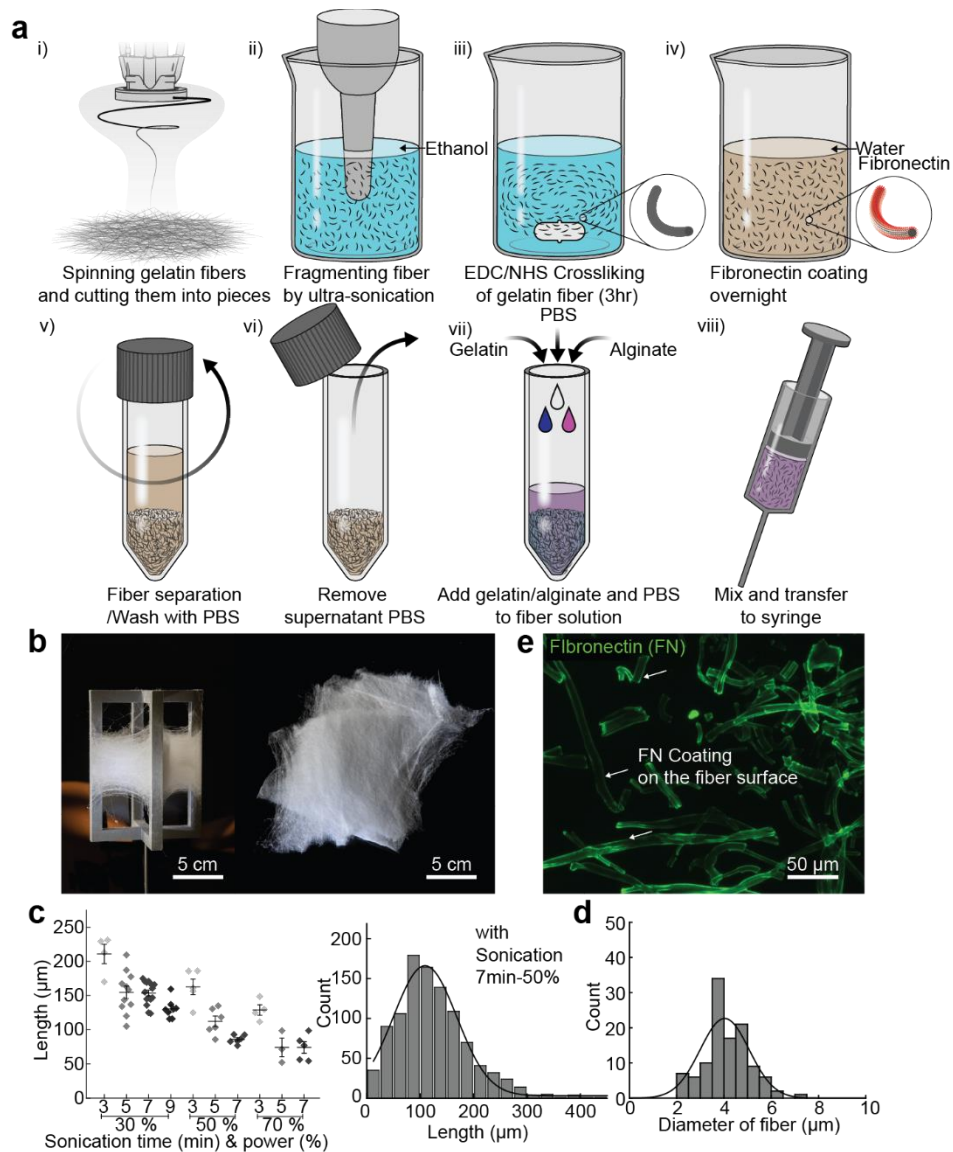
Supplementary Fig. 1. Preparation of gelatin fiber infused gel (FIG) inks and their components. a, Schematic illustration of the fabrication process of FIG ink. Detailed description in Methods. **b**, Gelatin fibers produced by focused rotary jet spinning. **c**, The average length of gelatin fibers varies when altering amplitude and time in the ultra-sonication process. n=4,11,15,8,5,6,6,4,3,5 batch average per condition. Data are presented as mean values +/- SEM (left). Distribution of fiber length when sonication was applied with power of 50% for 7 min (right). **d**, Distribution of fiber diameter in the FIG ink. **e**, Fibronectin coating of the gelatin fibers was confirmed using fluorescently labeled fibronectin.

Supplementary Fig. 2. Rheological properties of FIG ink depending on the fiber concentrations. a, A schematic illustration of the FIG inks as fiber concentration is diluted and concentrated. At a concentrated regime, the formation of the fiber-fiber network increases the solid-like behavior of the FIG inks. **b**, Storage (G′) and loss (G″) moduli as a function of oscillation stress depending on the fiber weight concentration of FIG inks. **c**, Stress-shear rate graph depending on the fiber concentration. Low yield stress of 0% fiber Gel-Alg hydrogel inks can be measured at the plateau. **d**, Yield stress depending on the fiber concentration was calculated at the cross-over point of the G′ and G″ shown in (b). n=3,4,4,4,3 inks per condition. Data are presented as mean values +/- SEM. Yield stress for 0 % fiber concentration was derived from the graph of the shear rate sweep test (c). **e**, tan δ (derived by G″/G′) moduli as a function of cyclic strain changes for 0, 5, 6, 8, and 10 wt% fiber of FIG inks, showing a clear sol-gel transition of 6 and 8 wt% as the storage and loss moduli intersect depending on the applied oscillation strain. 0 wt% shows only liquid-like behavior (tan δ>1) and 10 wt% only showed solid-like behavior due to much higher G′ at rest than other compositions. **f**, G′ changes of the FIG inks as a function of temperature for each fiber concentration. The higher G′ at the lower temperature enables the printing of 3D free-standing objects. **g**, 3D Printing results showing the effect of fiber concentration in 3D printability. While the FIG inks with 8 wt% fiber maintain the 3D ventricle structure after printing at 6 °C of printing bed temperature, its structure with the 6 wt% fiber of FIG inks collapses due to its less solid-like behavior at the same printing bed temperature. **h**, Viscosity changes as a function of shear rate for each fiber concentration of the FIG inks. **i**, *n* indexes depending on the fiber concentration derived from slopes of viscosity-shear rate graph (h) by power-law equation $\eta(\dot{\gamma}) = K\dot{\gamma}^{n-1}$, where η is viscosity, K is consistency index (defined as the viscosity at the shear rate of 1 s⁻¹), $\dot{\gamma}$ is the shear rate, and n is the shear-thinning index. n=5,4,5,5,5 inks per condition. Data are presented as mean values +/- SEM.

4
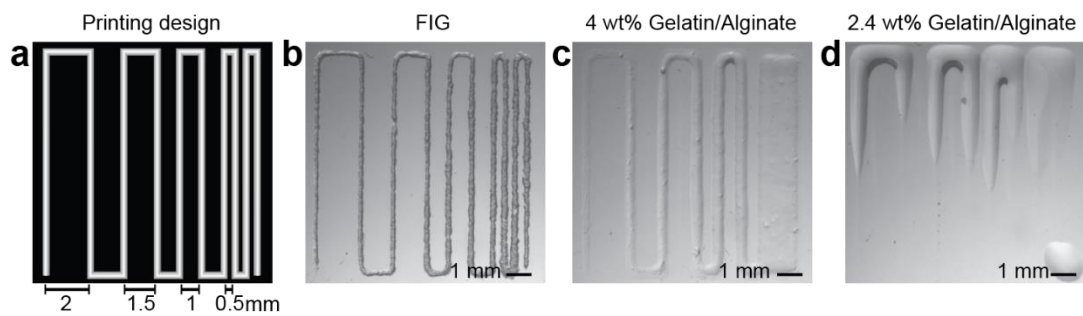
Supplementary Fig. 3. **Comparison of ink printability with variable line spacing pattern.**
**a-b**, FIG ink (8 wt% fiber, 2.4 wt% gelatin, 2.4% alginate) printed at a printing pressure of 130 kPa and a printing speed of 10 mm/s, showing a clear line shape (b) as it is designed (a). **c**, 4 wt% Gelatin/Alginate ink printed at a pressure of 55 kPa and a speed of 10 mm/s, showing a line shape at large spacing and merged lines at a narrow spacing. **d**, 2.4 wt% Gelatin/Alginate ink printed with a pressure of 40 kPa and a speed of 10 mm/s, showing a non-uniform line pattern.
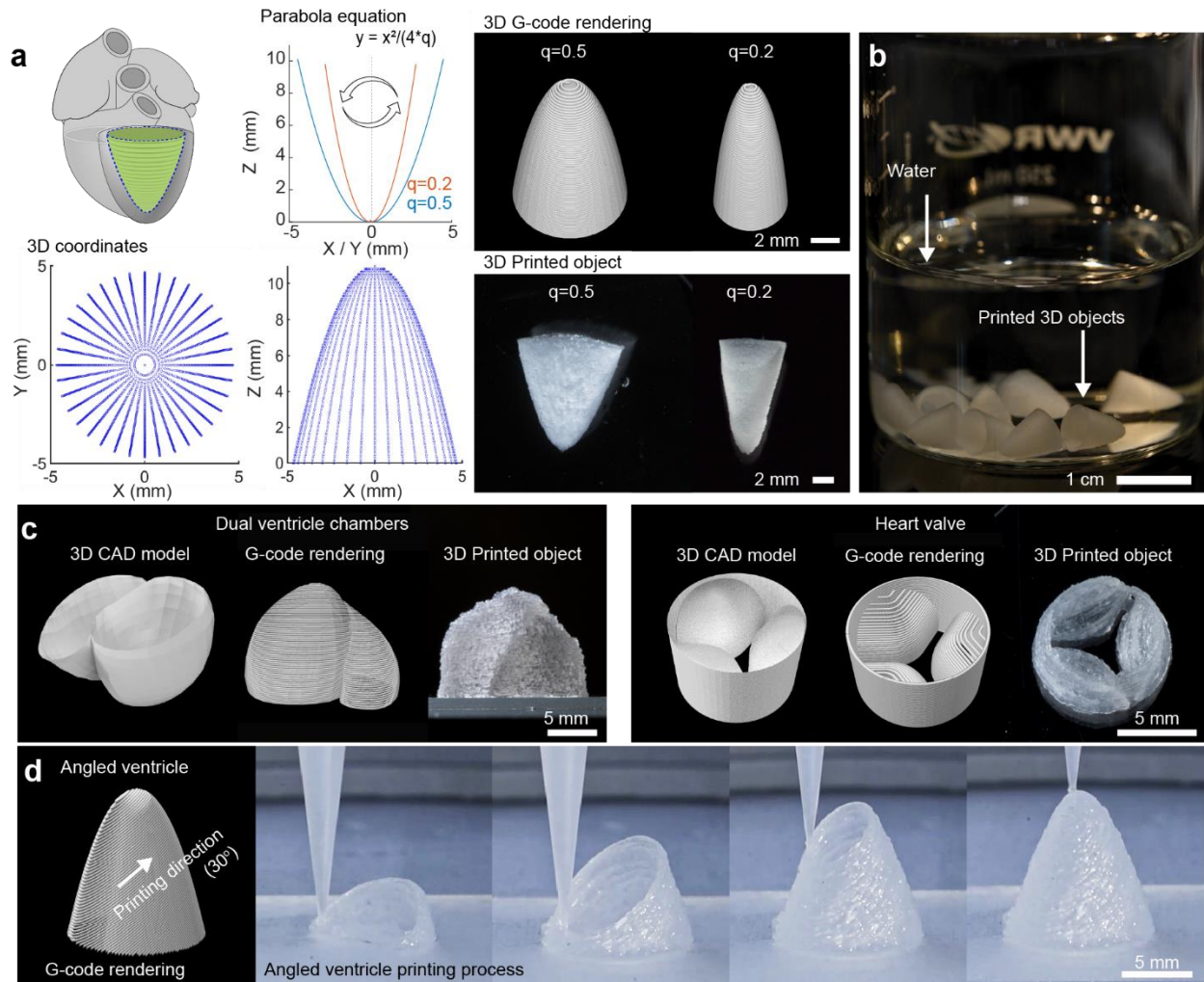
Supplementary Fig. 4. High shape retention of FIG inks allowing 3D self-supportive model of the heart. **a**, Design of printed ventricle chamber model using parabolic equation. 3D coordinates of the left ventricle can be derived by rotating a parabolic graph. 3D G-code render images showed printing pathways organized from 3D coordinates (top, right) and 3D printed objects were printed by corresponding G-code files (bottom, right). **b**, 3D printed FIG scaffolds were produced repeatedly and maintained their structure in water after crosslinking and calcium chelation processes. **c**, 3D self-supportive structure of a dual ventricle chamber model and a heart valve shown with 3D CAD model (left) and G-code rendered model (middle), and printed model (right). **d**, An angled ventricle model with a printing direction of 30°.
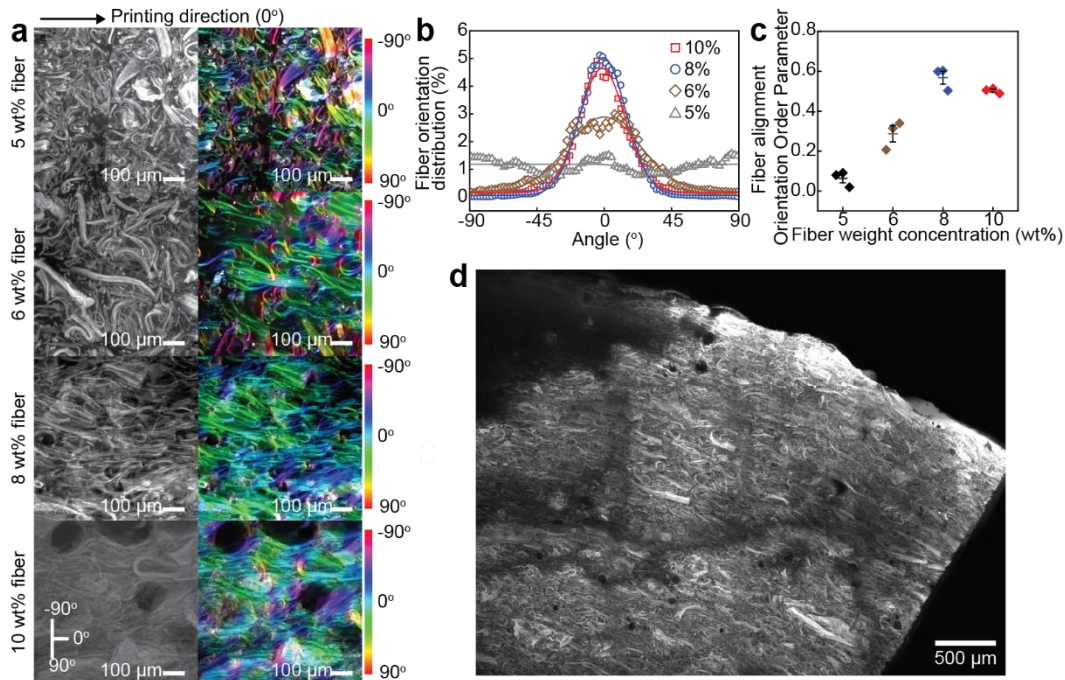
Supplementary Fig. 5. Fiber alignment in the 3D printed ventricle scaffolds. **a**, Representative confocal images of fibers in the 3D printed ventricle scaffolds at different fiber concentration and their corresponding images colorized by fiber angle on a range of -90º to 90º. 0º represents the printing direction. **b,** Fiber orientation angular distribution of the 3D printed FIG scaffolds with 5, 6, 8, and 10 wt% fibers.0º indicates the printing direction. 0º indicates the printing direction. Lines are gaussian fitting curves. 20~30 µm of Z stacks were max projected using Image J. **c**, Orientation order parameter (OOP) of fiber alignments from 3D printed ventricle scaffolds using different fiber concentrations of FIG inks. OOP value ranges from zero (random organization) to one (perfect alignment). n=3 3D printed structure per fiber conentration condition. Data are presented as mean values +/- SEM. **d**, A tilescan image of confocal microscope images showing large areas of fiber alignments from an excised 3D ventricle scaffold. 180 µm of Z stacks were max projected using Image J.
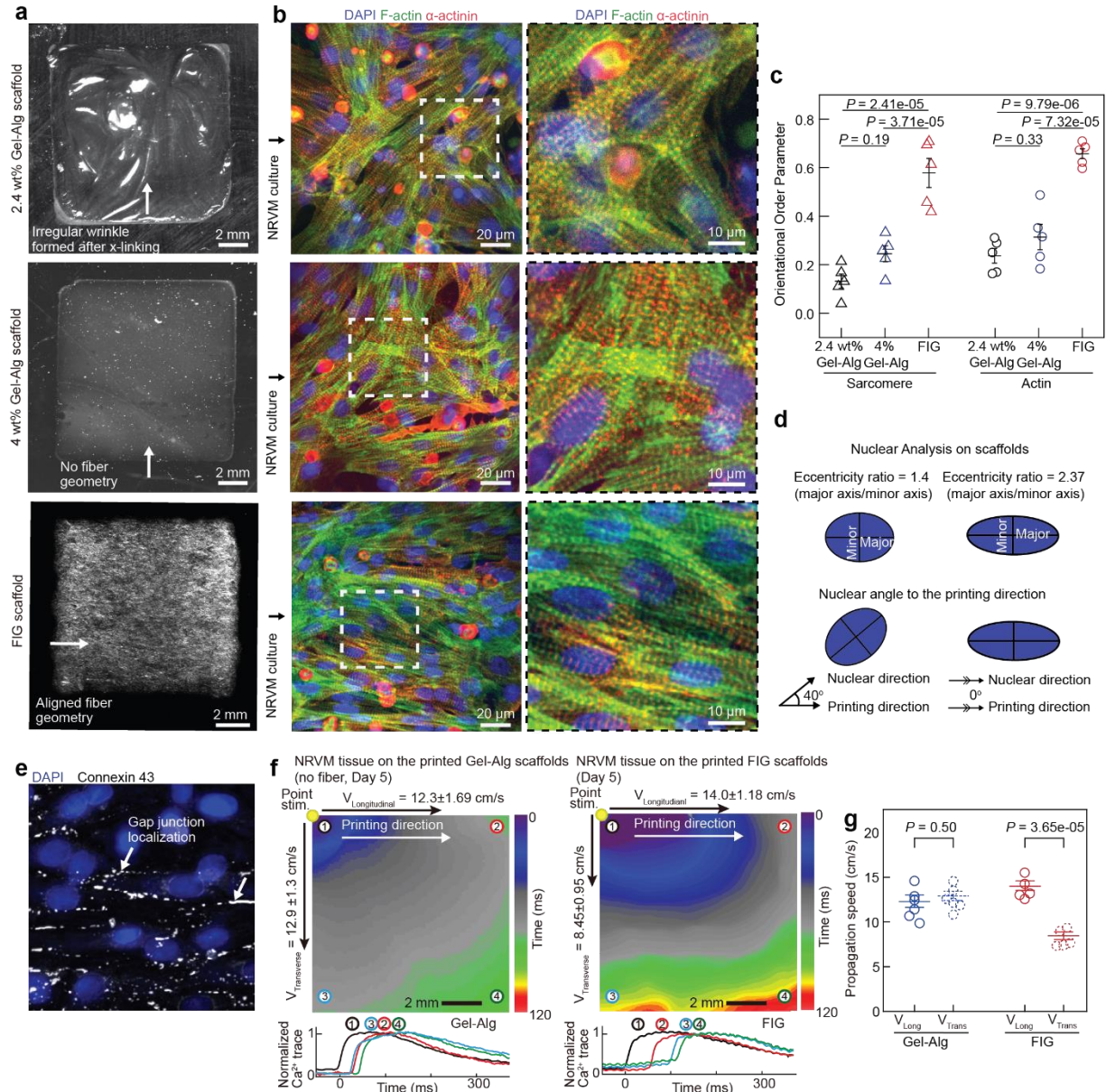
Supplementary Fig. 6. Structural and electrical anisotropy of *in vitro* cardiac tissues on FIG printed scaffolds. a, Darkfield images of 2D printed scaffolds using 2.4 wt% Gel-Alg hydrogel inks, 4 wt% Gel-Alg hydrogel inks and FIG inks with 2.4 wt% Gel-Alg and 8 wt% fiber. **b**, Immunostained images of nuclei (blue), α-actinin (red), and, F-actin (green) from NRVM tissue cultured (Day 5) on each scaffold shown in (a). **c,** Normalized sarcomeric α-actinin and F-actin alignment with their alignment quantified on a scale of 0 (random) to 1 (aligned) using an orientation order parameter. Statistical analysis was performed using one-way ANOVA with Tukey post-hoc test. n=5 tissues per scaffold condition. **d,** A schematic illustration showing the analysis method of nuclear eccentricity ratio (top) and alignment (bottom) with representative example. **e**, An immunostained image of connexin 43 (grey), Nuclei (blue) from NRVM tissue on the FIG. **f**, Isochronal map of Ca^{2+} transient propagations of the NRVM tissue (Day 5) on the printed Gel-Alg hydrogel scaffold (without fiber) and FIG scaffolds showing isotropic and anisotropic propagation, respectively. **g**, The ratio of longitudinal and transverse conduction

8

velocity, demonstrating anisotropic Ca^{2+} transient propagation occurred in the NRVM tissues on a printed FIG scaffold at day 5. Statistical analysis was performed using a two-tailed student's *t*-test with unequal variance, *****P=3.65e-05. n = 6 tissues on Gel-Alg scaffolds and n= 5 tissues on FIG scaffolds. All Data are presented as mean values +/- SEM.
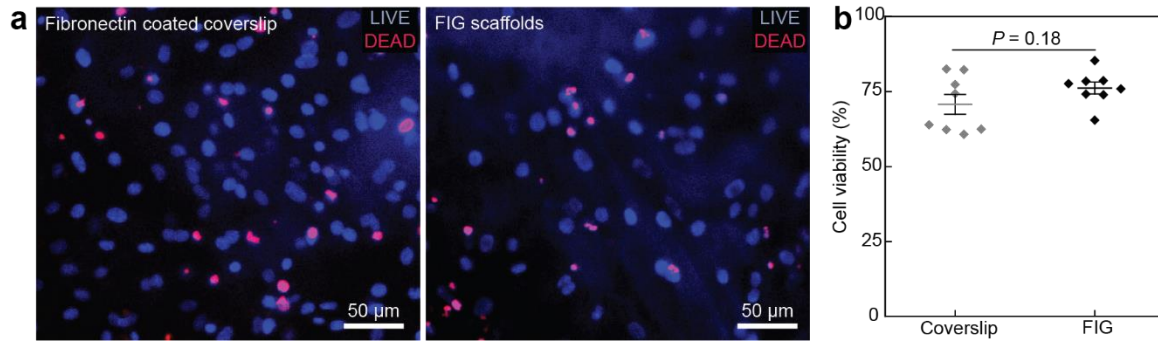
Supplementary Fig. 7. Live/Dead cell assays. a-b, Live/dead staining of NRVMs cultured on a fibronectin-coated coverslip (control, left) and a FIG scaffold (right) for 96 hrs (a), showing no significant differences (b). Error bar, SEM. Statistical analysis was performed using a two-tailed student's *t*-test with unequal variance, *P* = 0.185. n= 8 tissues per condition. Data are presented as mean values +/- SEM.
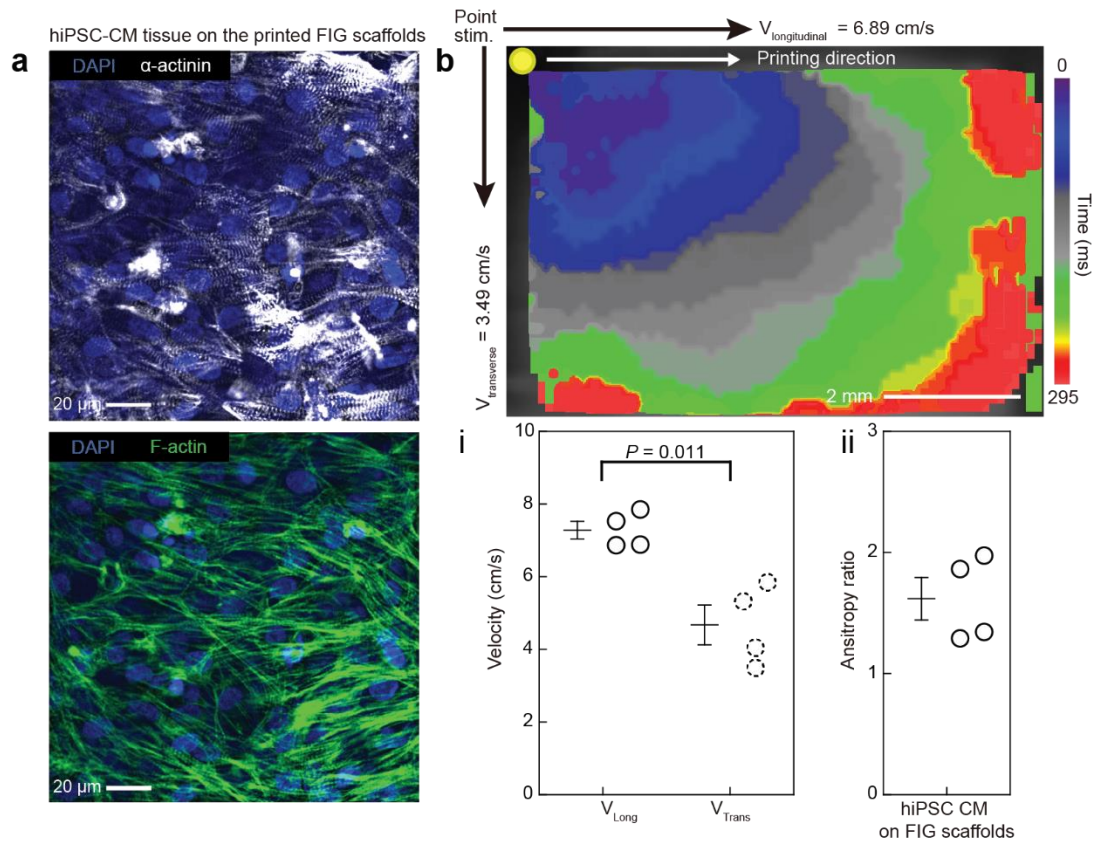
Supplementary Fig. 8. Anisotropic *in vitro* hiPSC-CM tissues on printed FIG scaffolds. a, A representative immunostained image of a hiPSC-CM tissue cultured on the printed FIG scaffold on day 7. **b**, hiPSC-CM tissues on a printed FIG scaffold have anisotropic Ca^{2+} propagation on day 7. Ca^{2+} transient conduction velocity in the longitudinal direction was significantly faster than that of in the transverse direction (i), resulting in their anisotropy ratio (V_{long}/V_{trans}) 1.62 ± 0.18 (mean $\pm$ SEM), (ii). Statistical analysis was performed using a two-tailed student's *t*-test with unequal variance, [*]$P = 0.011$. n = 4 tissues. Data are presented as mean values +/- SEM.
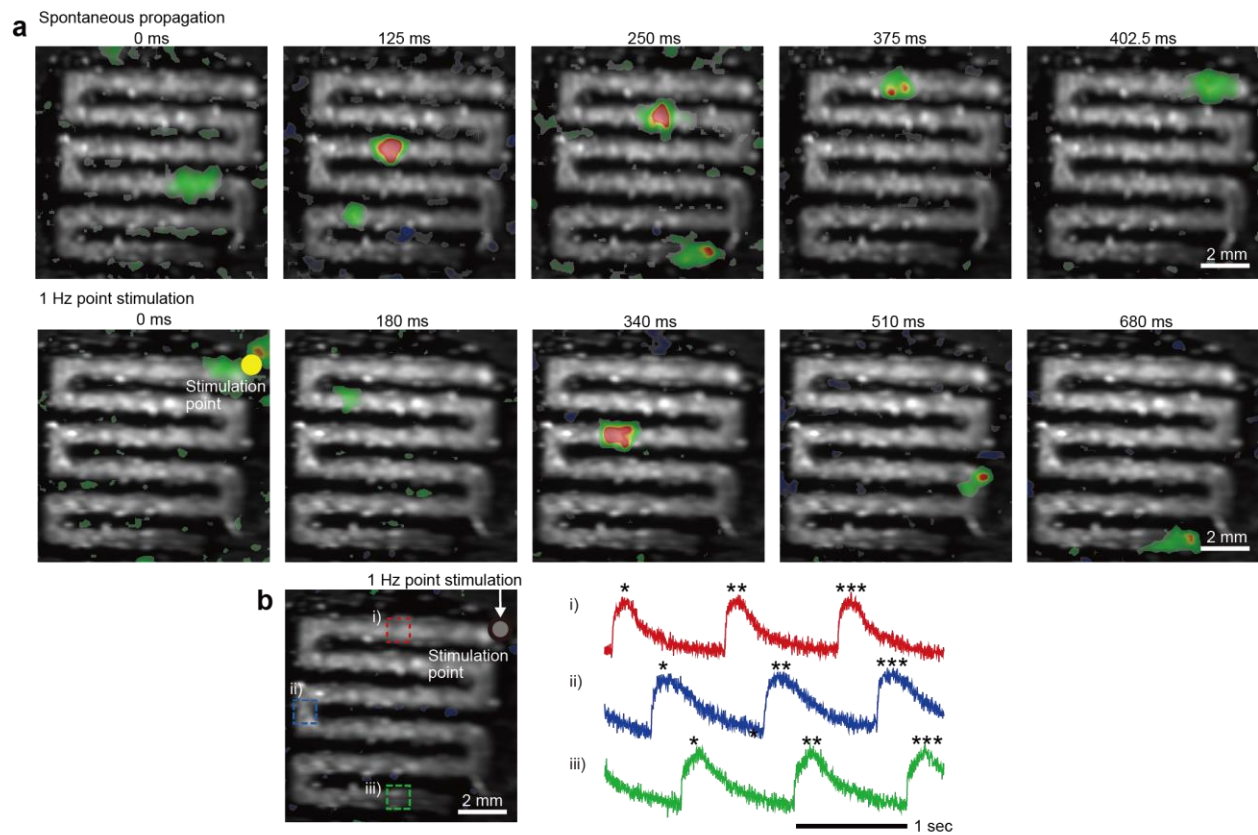
Supplementary Fig. 9. Sequential muscle activation of *in vitro* cardiac tissue on the printed pattern. a, NRVM tissue on serpentine printed patterns of FIG on day 11. Ca^{2+} transient propagation occurred along the patterned tissue. **b**, Ca^{2+} traces recorded at the points labeled in the left panel show the different activation time along the pattern. Annotation marks correspond to the same wavefront propagation. Continuous Ca^{2+} propagation is shown along the serpentine pattern in the Supplementary Video 5.
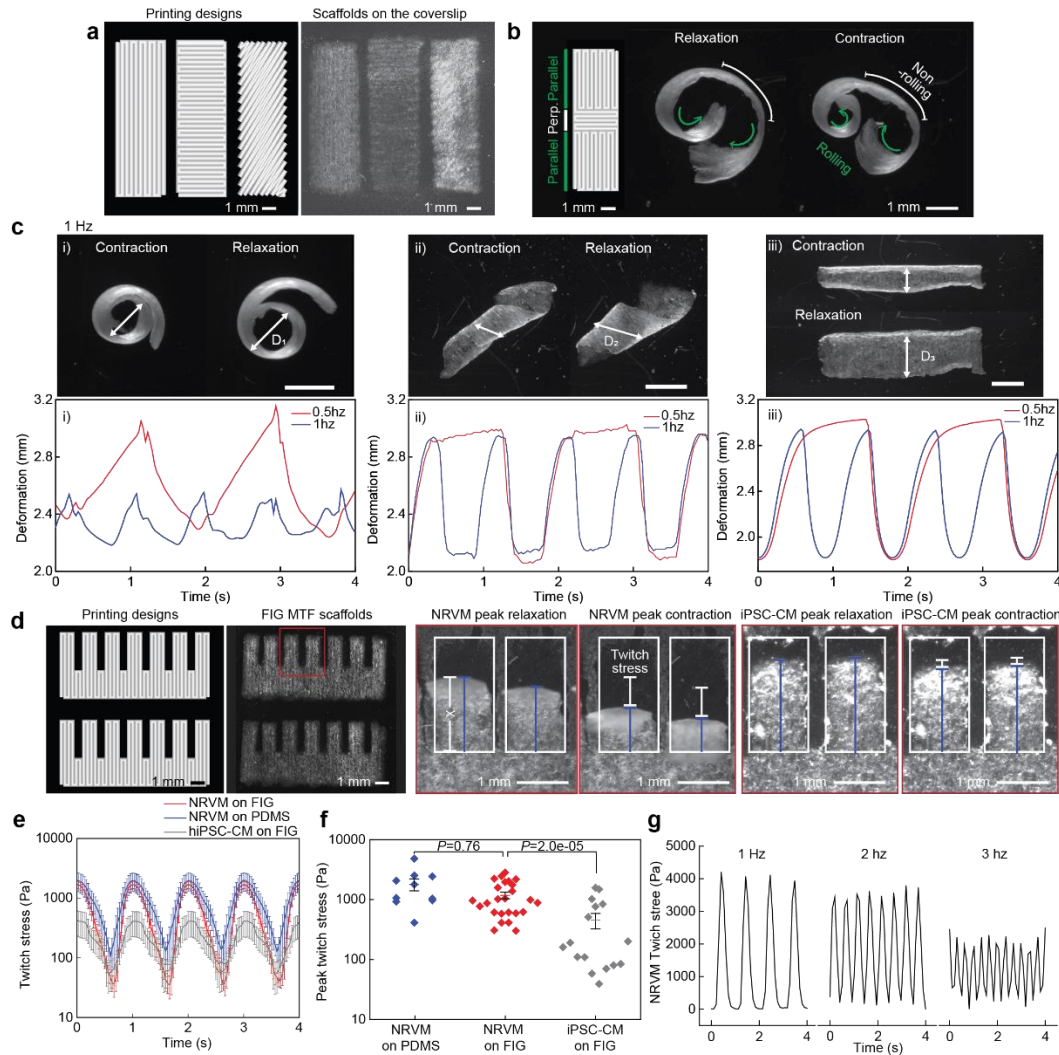
Supplementary Fig. 10. NRVM tissue contractility on the FIG scaffolds. a, Printing designs and printing result of rectangular shape with a size of 10 mm x 3 mm scaffolds printed with parallel, perpendicular, and angled directions. **b**, NRVM tissues cultured on the scaffold with alternative patterns with parallel and perpendicular printing directions, demonstrating local tissue contraction along the printing direction. **c,** Diameter changes in time by contraction of cardiac tissues aligned in parallel (i), angled (ii), and perpendicular (iii) direction to the long side of rectangular scaffolds under 0.5 Hz and 1 Hz field electrical stimulation. **d**, Printed FIG muscular thin films (MTF) platform to measure NRVM and iPSC-CM contractile stress. Projected cantilever bending distance (white arrow) converted into NRVM twitch stress. **e-f**, Average of twitching stress (e) and peak twitch stresses (f) of NRVM tissue on the FIG scaffolds, NRVM tissues on the fibronectin microcontact printed PDMS scaffolds, and hiPSC-CM tissues on the FIG scaffolds were measured under 1Hz field electrical stimulation. Statistical analysis was performed using a two-tailed student's *t*-test with unequal variance, *P*=0.76 for n.s, (not significant), ****P*=2.0e-05. n = 10, 25, 16 per cantilevers from 3,4,3 tissues. Data are presented as mean values +/- SEM. The thickness of PDMS, 20 µm; FIG, 70 µm; The modulus of PDMS, 2.14 MPa[3]; FIG, 51 kPa. **g,** A representative twitching stress changes of NRVM tissue on the FIG MTF in response to 1-3 Hz of field electrical stimulation.
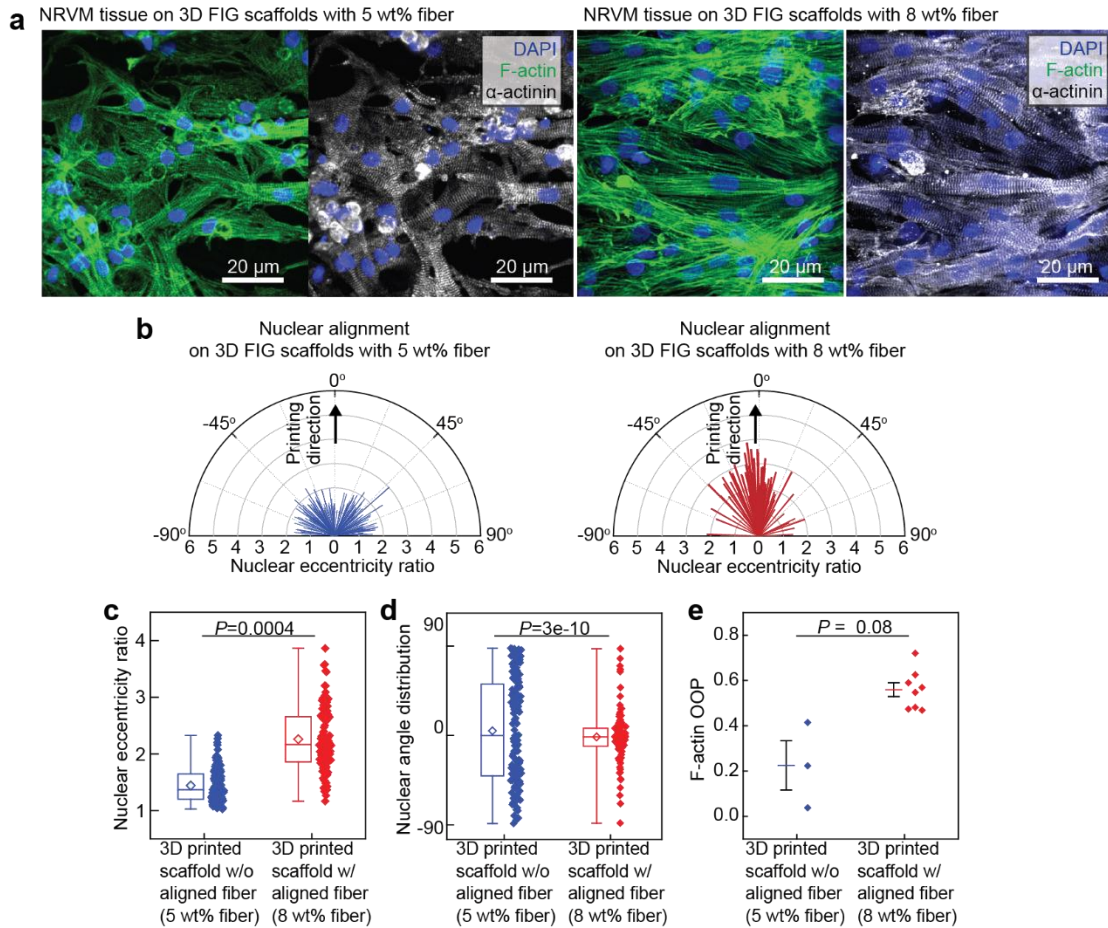
Supplementary Fig. 11. NRVM tissue alignment based on the fiber alignment on the printed 3D ventricle model. a, Immunostained images of NRVM tissue on the 3D printed ventricle using FIG inks with 5 wt% and 8 wt% fiber. Due to the low fiber alignment of 5 wt% FIG ink, NRVM tissues also show the random alignment of sarcomere and F-actin. **b**, Representative distribution of nuclear shape and orientation from NRVM tissues cultured on printed ventricle scaffolds with 5 wt% and 8 wt% FIG inks. **c-d**, Analysis of nuclear eccentricity ratio (c) and normalized nuclear angle (-90° to 90°; (d)) from NRVM tissues cultured on the 3D printed ventricle using FIG ink with 5 wt% and 8 wt% fiber. Statistical analysis was performed using a two-tailed student's *t*-test with unequal variance and a two-sample Kolmogorov-Smirnov test for (c) and (d) respectively, ****P=0.0004, *****P=3e-10. n= 147 and 100 nuclei from 4 tissues on 5 wt% and 8 wt% 3D FIG scaffolds, respectively. Box plot: center diamond, box limits, and whiskers indicate mean, the first and third quartiles, and max-min, respectively. **e**, Quantification of F-actin alignment using orientational order parameter (OOP) for NRVM tissue on the printed 3D FIG scaffolds with 5 wt% and 8 wt% fiber. Statistical analysis was performed using a two-tailed student's *t*-test with unequal variance. n= 3,8 tissues per condition. Data are presented as mean values +/- SEM.
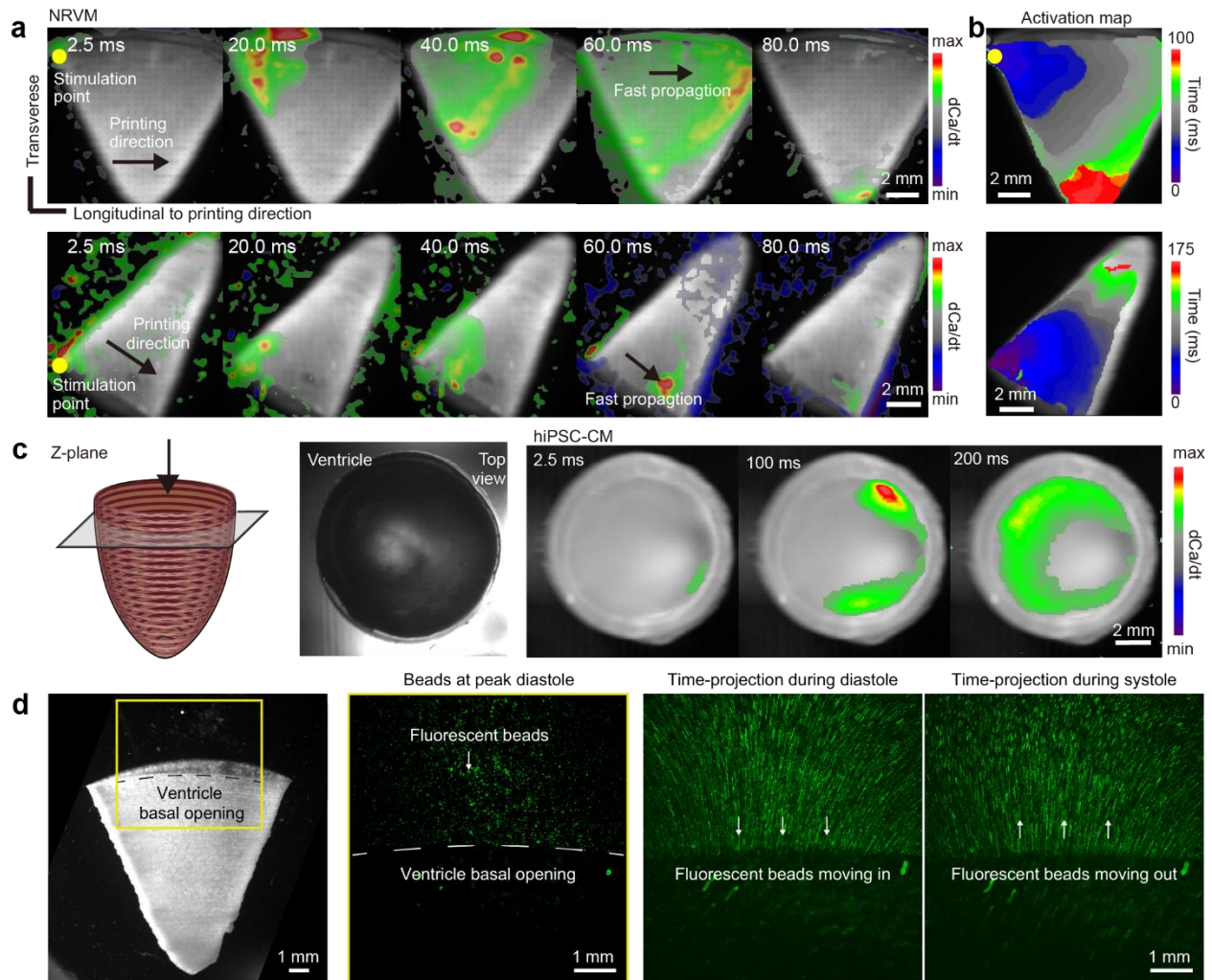
Supplementary Fig. 12. Synchronized and coordinated contractions of a tissue-engineered 3D ventricle model. a, Ca^{2+} transient propagations of NRVMs on the 3D printed ventricle scaffolds with representative wide- (top) and narrow-open (bottom) shapes under 1 Hz point stimulation. **b**, Isochronal map of Ca^{2+} transient propagations of NRVMs on the 3D wide- (top) and narrow-open (bottom) *in vitro* ventricle models. **c**, Spontaneous Ca^{2+} transient propagations of hiPSC-CMs on the 3D printed ventricle scaffold observed from the top, showing directional conduction throughout the 3D *in vitro* ventricle model. **d**, Contractility measurement of *in vitro* hiPSC-CM ventricle model using particle imaging velocimetry (PIV) in response to 1 Hz of field electrical stimulation. Time-projection image shows tracking images of fluorescent beads movement during relaxation (time: 0.56 s) and contraction (time: 0.462 s).

Supplementary Video. 1.

Direct 3D printing ventricle-shaped scaffolds without using supporting materials.

Supplementary Video. 2.

Beating iPSC-CMs after the differentiation process is finished.

Supplementary Video. 3.

Optical mapping images for the Ca^{2+} transient propagation of NRVM tissues cultured on the printed Gel-Alg hydrogel (left) and FIG scaffolds (right). 1Hz point electrical stimulation was applied at the left top corner of each tissue.

Supplementary Video. 4.

Optical mapping images for the Ca^{2+} transient propagation of hiPSC-CM tissues cultured on the printed FIG scaffolds under 1 Hz (left) and 2 Hz (right) point electrical stimulation at the left top corner.

Supplementary Video. 5.

Optical mapping images for the Ca^{2+} wave propagation occurred through the printed FIG patterns, showing sequential muscle activation.

Supplementary Video. 6.

Contraction of NRVM tissue on the 3D printed rectangular scaffolds printed in parallel, angled, and perpendicular directions to the long side of scaffold geometry, showing different contractile motion, rolling, twisting, and bending, respectively under 0.5Hz field electrical stimulation.

Supplementary Video. 7.

Spontaneous contraction of 3D *in vitro* human iPSC-CM ventricle model in the RPMI/B27(-) media.

Supplementary Video. 8.

Spontaneous contraction of 3D *in vitro* NRVM ventricle model in Tyrode's solution.

Supplementary Video. 9.

Ca^{2+} transient propagation from 3D *in vitro* NRVM ventricle model under 1Hz point electrical stimulation. The point stimulation was applied where the propagation started.

Supplementary Video. 10.

Spontaneous Ca^{2+} transient propagation from 3D *in vitro* human iPSC-CM ventricle model observed at the top, middle, and bottom plane.

Supplementary Video. 11.

Deformation mapping analysis from 3D *in vitro* human iPSC-CM ventricle model. Movement of fluorescent beads adhered on the ventricle (left panel) was analyzed during systole and diastole cycle of the 3D *in vitro* ventricle tissue model (right panel).

Supplementary Video. 12.

Contractility assessment of a 3D *in vitro* human IPSC-CM ventricle tissue model using PIV analysis. Brightfield micrograph of 3D *in vitro* human iPSC-CM ventricle model (left) with green region of interest (ROI) region box (left), fluorescent beads movement from the corresponding ROI (top, right), and phase averaged velocity map from the ROI region (bottom, right).

Supplementary references

1.   Mueller, S., Llewellin, E. W., Mader, H. M. The rheology of suspensions of solid particles. *Proc. R. Soc. A* 466, 1201-1228 (2009)
2.   Chaouche, M., Koch, D. L. Rheology of non-brownian rigid fiber suspensions with adhesive contacts. *J. Rheol.* 45, 369-382 (2001)
3.   Johnston, I. D., McCluskey, D. K., Tan, C. K. L., Tracey, M. C. Mechanical characterization of bulk sylgard 184 for microfluidics and microengineering. *J. Micromech. Microeng.* 24, (2014)